Structural, magnetic, and electronic properties of VxCr2–xS3(0 <x< 2)

Article

Accepted Version

Structural, Magnetic, and Electronic Properties of $V_xCr_{2-x}S_3$ (0<x<2)

T. Erinc Engin[a], Anthony V. Powell[*a] and Steve Hull[b]

[a]Department of Chemistry, Heriot-Watt University,

Edinburgh EH14 4AS, UK

[b]ISIS Facility, Rutherford Appleton Laboratory, Didcot,

Oxfordshire OX11 0QX, UK

*Correspondence to:
Dr A.V. Powell
Department of Chemistry
Heriot-Watt University
Edinburgh EH14 4AS
UK
Fax: +44 (0)131 451 3180
E-mail: a.v.powell@hw.ac.uk

Abstract

A new family of vanadium-substituted chromium sulphides ($V_xCr_{2-x}S_3$, $0<x<2$) has been prepared and characterised by powder X-ray and neutron diffraction, SQUID magnetometry, electrical resistivity and Seebeck coefficient measurements. Vanadium substitution leads to a single-phase region with a rhombohedral Cr_2S_3 structure over the composition range $0.0<x\leq0.75$, whilst at higher vanadium contents ($1.6\leq x<2.0$) a second single-phase region, in which materials adopt a cation-deficient Cr_3S_4 structure, is observed. Materials with the Cr_2S_3 structure all exhibit semiconducting behaviour. However, both transport and magnetic properties indicate an increasing degree of electron delocalisation with increasing vanadium content in this compositional region. Materials that adopt a Cr_3S_4-type structure exhibit metallic behaviour. Magnetic susceptibility data reveal that all materials undergo a magnetic ordering transition at temperatures in the range 90-118K. Low-temperature magnetization data suggest that this involves a transition to a ferrimagnetic state.

T. Erinc Engin, Anthony V. Powell, and Steve Hull

Chem. Mater.

Structural, Magnetic, and Electronic Properties of $V_xCr_{2-x}S_3$ ($0<x<2$)

$V_xCr_{2-x}S_3$ exhibits two single-phase regions. Above x=1.6, materials are metallic and below x=0.75, semiconducting. The electrical resistance of semiconducting phases decreases with x, due to preferential occupation of sites in a dichalcogenide block by vanadium, resulting in increased electron delocalisation. Magnetic order is observed in both single-phase regions.

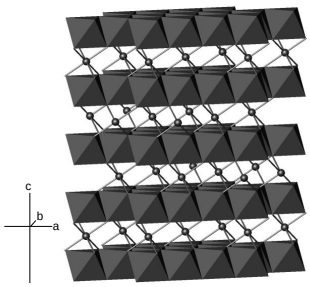

Introduction

The structures of ternary chalcogenides of the type A_yMX_2 ($0 \leq y \leq 1$) consist of MX_2 layers of edge-sharing octahedra, between which there is a network of octahedral sites. At the compositional extreme, y=0, these sites are vacant and the structure adopted is that of CdI_2 in which layers of edge-sharing MX_6 octahedra are separated by a van der Waals' gap. At the other limit, y=1, complete occupancy of octahedral sites between MX_2 layers leads to the NiAs structure in which metal-centred octahedra share faces as well as edges. Between these compositional extremes, occupancy of a fraction of the octahedral sites in the van der Waals' gap by *A*-cations may lead to ordering of vacancies within the partially occupied layer. This gives rise to a variety of two-dimensional superstructures[1,2,3] whose relative stability depends on y.

Many binary and ternary transition metal chalcogenides adopt such ordered-defect structures.[4,5,6,7,8] Within the chromium-sulphur system, this includes the M_2S_3 (y=1/3) and M_3S_4 (y=1/2) structure types, for which the vacancy ordering schemes are shown schematically in Figure 1. In Cr_2S_3 (Figure 2), vacancy ordering produces a supercell with dimensions related to those of the primitive hexagonal subcell by $\sqrt{3}a_p x \sqrt{3}a_p \times 3c_p$. Cr_2S_3 is ferrimagnetic[9,10] with $T_c \approx 125K$, the temperature at which an anomaly is observed in the transport properties.[11] The interaction between charge carriers and localized magnetic moments leads to an exchange splitting of the conduction band and it has been suggested that spin-disorder scattering of the charge carriers is responsible for this anomaly.[11] Sulphur deficiency markedly reduces the resistivity of the semiconducting phase, introducing a local maximum into ρ(T)

at temperatures in the region of the ferrimagnetic ordering temperature, T_C. Compositions that exhibit this resistivity anomaly exhibit a negative magnetoresistance that peaks at T_C and attains a maximum of 48% in $Cr_2S_{2.92}$.[12]

By contrast, V_2S_3 adopts a cation deficient M_3S_4 (y=1/2) structure[7] (Figure 3). Occupancy of half of the octahedral sites between MX_2 units gives rise to a $\sqrt{3}a_p \times a_p \times 2c_p$ supercell and an M_3X_4 stoichiometry. However, this structure can tolerate significant levels of non-stoichiometry whilst retaining the same supercell.[13,8] In the vanadium-sulphur system, the non-stoichiometry extends to a composition of V_2S_3 in which, in addition to the 50% of available octahedral sites between MS_2 units that are vacant in the M_3S_4 structure, further cation vacancies are randomly distributed over the 50% of occupied sites. This reduces the cation:anion ratio from 0.75 to 0.67. This material may thus be formulated $(M)_{0.67}[M]_2S_4$, where parentheses and square brackets represent sites in the vacancy and fully-occupied layers respectively.

In this work, the effect on the structural, electron transport and magnetic properties of the progressive substitution of chromium in Cr_2S_3 by vanadium is explored. A new series of materials of the general formula $V_xCr_{2-x}S_3$ ($0<x<2$) has been prepared that exhibits more complex phase behaviour than the Cr_3S_4-type analogues reported previously.[14,15,16]

Experimental

Mixtures of vanadium (Alfa Aesar, 99.5%), chromium (Alfa Aesar, 99.95%) and sulphur (Sigma-Aldrich, 99.998%) powders, corresponding to

stoichiometries $V_xCr_{2-x}S_3$ with $0 < x < 2$, were ground in an agate mortar and sealed into evacuated ($<10^{-4}$ Torr) silica tubes. Prior to use, the vanadium powder was washed with dilute hydrochloric acid to remove a green coating of oxide. Reaction mixtures were heated initially at 500 °C for 24 h, reground and then refired for a total of 7d with one intermediate regrinding. Products were cooled to room temperature at 0.8 °C min^{-1}, prior to removal from the furnace. Pellets of the materials for electron-transport measurements were made by pressing the sample under 10 tons of pressure before sintering in a sealed evacuated silica tube at 800 °C.

Powder X-ray diffraction data were collected using a Philips PA2000 diffractometer with nickel-filtered Cu-K_α radiation (λ=1.5418 Å). Data were collected over the angular range $10 \leq 2\theta/^\circ \leq 100$, counting for 5s at each 0.02° increment in 2θ. Time-of-flight powder neutron diffraction data were collected at room temperature on the Polaris diffractometer at the ISIS Facility, Rutherford Appleton Laboratory. Samples (*ca*. 3 g) were contained in thin-walled vanadium cans. Initial data manipulation and reduction was carried out using the Genie[17] spectrum manipulation software. Neutron diffraction data, from the highest resolution backscattering bank of detectors ($130 \leq 2\theta/^\circ \leq 160$), were summed and normalized for subsequent use in conjunction with X-ray data in Rietveld refinement using the GSAS package.[18]

The electrical resistance of the samples was measured over the temperature range $77 \leq T/K \leq 300$ using a 4-probe DC technique. An ingot (~6 x 3 x 1 mm) was cut from a sintered pellet, four 50 μm silver wires were attached using colloidal silver paint and connections were made to a HP34401A multimeter.

The sample was mounted in an Oxford Instruments CF1200 cryostat connected to an ITC502 temperature controller. Measurements were carried out over the temperature range 77≤T/K≤300.

Determination of the Seebeck coefficient over the temperature range 80≤T/K≤350 was carried out using equipment constructed in-house. Two 50 μm copper wires were attached with silver paint to each end of a sintered ingot (*ca.* 10 x 4 x 1mm) of material, and connections made to a Keithley 2182 nanovoltmeter for the measurement of the thermal voltage. The sample was mounted on a holder which incorporates a heater that allows a temperature gradient to be created across the sample. Two Au:0.07%Fe *vs*. chromel thermocouples connected to an ITC503 temperature controller (Oxford Instruments), were placed in contact with the sample at each end of the ingot. This assembly was located in an Oxford Instruments CF1200 cryostat connected to an ITC502 temperature controller. Data were collected in 5K increments over the temperature range 80≤T/K≤300. At a given temperature, the Seebeck coefficient was determined by increasing the temperature of one end of the sample and measuring the voltage, ΔV, as a function of the temperature difference, ΔT, across the sample. The Seebeck coefficient is then determined from the gradient $\Delta V/\Delta T$. Values were corrected for the effects of the Cu wires.[19]

Magnetic susceptibility measurements were performed using a Quantum Design MPMS2 SQUID susceptometer. Samples were loaded into gelatin capsules at room temperature and data were collected over the temperature range 5≤T/K≤300, both after cooling in zero applied field (zfc) and in the

measuring field (fc) of 1000 G. Data were corrected for the diamagnetism of the gelatin capsule and for intrinsic core diamagnetism. Magnetization data were obtained at 5K over the field range 0≤H/G≤10000 in 1000 G steps after cooling in zero-field.

Results and Discussion

Powder X-ray diffraction data reveal that materials in the composition range $0<x\leq0.75$ adopt the rhombohedral Cr_2S_3-type structure of the end-member phase. Increasing the vanadium content leads to a two-phase mixture of R-Cr_2S_3 and monoclinic Cr_3S_4-type phases until, for compositions above x=1.6, a second single phase region corresponding to the monoclinic Cr_3S_4-type, is observed.

Powder X-ray and neutron diffraction data were used simultaneously in Rietveld analysis in order to determine the distribution of chromium and vanadium ions amongst sites in the defective and fully occupied layers. This approach exploits the high degree of contrast between the two cations in powder neutron diffraction, due to the vanishingly small neutron scattering length of vanadium, whilst overcoming the difficulties the latter presents in locating vanadium directly by neutron methods alone. Neutron data in the time-of-flight range 3000-19300 μs (d ≈0.5-3.2 Å) were used together with X-Ray data in the angular range 20-100° (d ≈1.0-4.4 Å). In order to facilitate comparison of data from the two techniques, units of d-spacing will be used throughout this work. Structural refinements for $V_xCr_{2-x}S_3$ ($0\leq x\leq0.75$) materials were initiated in the space group $R\bar{3}$ and those for materials in the

composition range 1.6≤x≤2.0 in *I2/m*, using atomic coordinates and lattice parameters from the previous X-ray diffraction study of Cr_2S_3 and Cr_3S_4 for the initial structural models.[6] In the trial structural models, vanadium and chromium occupied the available sites in a statistical manner. Neutron scattering lengths and X-ray scattering factors incorporated within the GSAS program were used. The backgrounds of both X-ray and neutron data were modelled using a cosine Fourier series with the coefficients included as refinable parameters. A pseudo-Voigt peak shape was used for X-ray data, whereas a more complex peak shape description involving the convolution of a Gaussian with a double exponential function was used for the neutron data. Regions centred at d =2.1–2.2, 1.5-1.6 and 1.2-1.3 Å in the neutron data were excluded from refinements owing to the presence of vanadium (d_{110} = 2.14 Å, d_{200}=1.52 Å and d_{211}=1.24 Å) originating from the sample can.

Following initial refinement of scale factors, background terms, X-ray zero-point, positional and lattice parameters, site occupancy factors and thermal parameters were introduced as variables into the refinement. In all cases, a single thermal parameter was used for the cations and for the anion. For materials with the M_3S_4-type structure, site occupancy factors of vanadium and chromium were allowed to vary with the constraint that the overall stoichiometry was maintained. For materials in the M_2S_3-type region there are three crystallographically-distinct cation sites (3(b), 3(a) and 6(c)) and an alternative strategy for refining of site occupancy factors was adopted. Initially the site occupancy factors for the two cations at the two sites in the fully occupied layer (6(c) and 3(a)) were allowed to vary with the constraint

that the overall stoichiometry of this layer was maintained. In order to allow for the possibility of redistribution of cations between fully occupied and vacancy layers, the site occupancy factor of the vacancy layer site was refined together with that of each of the two sites in the fully occupied layer in turn. In each case a constraint was applied to maintain the nominal stoichiometry. This procedure led to a significant improvement in quality of the fit as the result of a redistribution of the cations from the statistical arrangement. Finally, the possibility that additional vacancies may be present in the vacancy layer was explored by allowing site occupancy factors of chromium and vanadium residing at the vacancy layer 3(b) site to vary freely. However, with the exception of the refinement for $V_{0.6}Cr_{1.4}S_3$, this did not lead to any appreciable deviation of the site occupancy factors at this site from their previously determined values. For the case of $V_{0.6}Cr_{1.4}S_3$, whilst this site remained fully occupied, there were small changes in the relative amounts of vanadium and chromium at this site, leading to a slightly altered stoichiometry of $V_{0.57}Cr_{1.43}S_3$. Following the introduction of peak shape parameters, the final cycle of refinement produced residuals in the range 12.51-17.61% (X-ray) and 1.07-2.73% (neutron). Refinements of an initial structural model in which the available vanadium was equally apportioned amongst vacancy and fully occupied layers converged at essentially the same cation distribution as that arrived at using the procedure described above. Observed, calculated and difference profiles representative of each single phase region are presented in Figure 4, whilst the remaining profiles are provided as supplementary

information. Final refined atomic parameters appear in Tables 1 and 2, whilst significant bond distances and angles are provided in Tables 3 and 4.

Examination of cation site-occupancy factors (Tables 1 and 2) reveals that across the composition range of the M_2S_3-type structure, the fraction of vanadium that resides in the fully occupied layer (V_F) increases with increasing vanadium content (Figure 6), reaching a value of *ca*. 63% at x=0.6, corresponding to a formulation $(V_{0.22}Cr_{0.28})[V_{0.38}Cr_{1.12}]S_3$. At the higher levels of vanadium incorporation corresponding to the M_3S_4-type phases, sites in the fully occupied layer are predominantly (*ca*. 80%) occupied by vanadium. This represents a significant difference from the behaviour of the analogous $V_xCr_{3-x}S_4$ phases,[20] in which there is a marked discontinuity in V_F as a function of vanadium content. For compositions with $x \geq 0.4$, the distribution conforms closely to the general formula $(V_{x/2}Cr_{(1-x/2)})[V_{x/2}Cr_{(2-x/2)}]S_4$, whilst below x=0.4, V_F decreases rapidly, leading to a near-normal distribution at x=0.2. We have proposed that[20] these site-preferences reflect the relative abilities of the cations present to delocalize electrons by direct t_{2g}-t_{2g} interactions and that the structure adopted is that which best balances the competition between electron delocalization and charge separation. In the present case, as both chromium and vanadium cations are trivalent, redistribution of cations does not lead to charge separation and therefore, it would be expected that electronic factors would favour the occupation of sites in the fully occupied layer by vanadium, as appears to be the case at higher vanadium contents, where the capacity for direct t_{2g}-t_{2g} interactions is greatest.

Examination of the compositional dependence of the unit-cell volume per M_2S_3 formula unit, (Figure 6(a)) reveals a marked discontinuity on going from the M_2S_3-type to M_3S_4-type structure. The in-plane dimensions of the M_2S_3-type phases ($0<x\leq0.75$) show only a slight decrease with increasing vanadium content, whilst the lattice parameter perpendicular to the dichalcogenide slabs increases almost linearly with x (Figure 6(b)). This trend is continued into the M_3S_4-type phases ($1.6\leq x\leq2.0$), whereas the in-plane dimensions, no longer constrained to be equivalent by symmetry, diverge at the phase boundary. The *b* lattice parameter appears to continue the trend established as the boundary of the M_2S_3 region is approached, whilst the *a* lattice parameter is significantly larger than would be expected by extrapolation of the behaviour in the M_2S_3 region. This divergence of the in-plane lattice parameters is reflected in the behaviour of the cation-cation distances within the fully-occupied layer. Each cation in this layer has six in-plane nearest neighbour cations. With increasing vanadium content, intralayer cation-cation distances decrease slightly, suggesting an increase in the strength of the cation-cation interactions, whilst retaining a near-hexagonal arrangement. However, for materials in the M_3S_4 compositional region, the six nearest-neighbour distances within the fully occupied layer fall into three pairs, one corresponding to the lattice translation along the b-axis, a second pair of cation-cation separations at a significantly longer distance and a third at a distance of *ca*. 3Å, below the critical distance, R_c, of 3.1Å estimated for direct t_{2g}-t_{2g} overlap. Intralayer distortions of this type, involving the formation of zigzag cation chains, have been observed in a number of mixed-metal

sulphides.[21,22] and have been shown to be associated with the onset of metallisation through the creation of a one-dimensional band of t_{2g}-derived states.

The formation of a t_{2g}-derived band, which for materials in the composition range $1.6 \leq x < 2$ is only partially filled, manifests itself in the electrical transport properties. The resistivity of materials with the M_3S_4-type structure (Figure 7) shows a relatively weak temperature dependence and a positive $d\rho/dT$, consistent with metallic behaviour. By contrast, the temperature dependence of the resistivity of materials in the composition region $0 \leq x \leq 0.75$ is indicative of semiconductivity. However, with increasing vanadium content, there is a progressive decrease in the resistivity. (Figure 7). Although the resistivity of $V_{0.75}Cr_{1.25}S_3$ is six orders of magnitude lower than that of $V_{0.1}Cr_{1.9}S_3$, the positive sign of $d\rho/dT$ indicates that semiconducting behaviour persists to the phase boundary. The marked decrease in resistivity on substitution of vanadium for chromium may be related to the creation of holes in the t_{2g} band, resulting from the replacement of Cr^{3+}:d^3 by V^{3+}:d^2, and to the band broadening that results from stronger cation-cation interactions.

Resistivity data for $V_{0.1}Cr_{1.9}S_3$ and $V_{0.2}Cr_{1.8}S_3$ follow Arrhenius-type behavior (Figure 8) above 166 K and 120 K respectively, yielding activation energies of 66.3(1) meV and 46.9(2) meV. These values are similar to those of 37(6) meV determined[23] for Cr_2S_3 and 44(1) meV obtained for a sulphur-deficient phase.[12] At higher levels of vanadium incorporation ($0.25 \leq x \leq 0.75$) plots of $\ln(\rho)$ *vs.* 1/T are non-linear indicating that the conduction mechanism is not of the Arrhenius type. However for materials in this composition range, a plot of

ln(ρ) *vs.* $T^{-1/4}$ is linear over the temperature range 80≤T/K≤300 (Figure 9) indicating a variable-range-hopping conduction mechanism[24,25] of the form

$$\rho = \rho_0 \exp\left[\left(\frac{T}{T_0}\right)^{\nu}\right] \quad (1)$$

with ν = ¼. Increasing levels of substitution of chromium introduces disorder, which may cause states at the band edge to become localized, while states in the band centre remain delocalized. As the Fermi energy lies on the localized side of the mobility edge, the conduction is then dominated by hopping of charge carriers between states localized on opposite sides of the Fermi energy according to the variable-range-hopping mechanism. The constant T_0 (Table 6), determined for the compounds in the variable-range-hopping regime (Equation 1), is given by[26], $T_0=21/k_BN(E_F)\xi^3$, where $N(E_F)$ is the density of states at the Fermi level and ξ is the localization length, which is a measure of the spatial extent of the wave function localized at a single site. An estimate of ξ was obtained by using a value of $N(E_F)$ = 1.6 × 10^{23} states/ eV cm^3 from band structure calculations for CrS.[27] The value of ξ so determined increases throughout the composition range 0.25≤x≤0.75, supporting the view that electrons are becoming increasingly delocalised as the level of vanadium incorporation increases.

A Seebeck coefficient of –325 μV K^{-1} has been reported[11] for the end-member phase, Cr_2S_3. Sulphur deficiency increases this slightly: a value of -391 μV K^{-1} being reported[12] for $Cr_2S_{2.92}$. This indicates that electrons are the dominant charge carriers in the binary phases. Substitution of Cr^{3+}:d^3 by V^{3+}:d^2 introduces holes into the conduction band, with the result that both electrons

and holes can contribute to the electrical conduction. The Seebeck coefficient of such a mixed conductor is then the conductivity-weighted sum of the contributions from electrons and holes. At low levels of vanadium incorporation, the Seebeck coefficient of $V_xCr_{2-x}S_3$ phases is positive (Figure 10), suggesting that hole-type conduction dominates. Furthermore, the relatively large room-temperature value of S exhibited by $V_{0.2}Cr_{1.8}S_3$ is consistent with the highly resistive nature of the material. As the vanadium content is increased through the M_2S_3-type region, the resistivity falls as a result of increasing electron delocalisation, and there is a concomitant reduction in the room temperature value of the Seebeck coefficient, until for compositions with $x \geq 0.5$, negative values are observed. This indicates that as the phase boundary is approached, electron conduction again begins to dominate, as the result of increased electron mobility due to band broadening. In the M_3S_4 region where resistivity data indicates metallic behaviour, $|S| < 10\ \mu V\ K^{-1}$: values that are typical of a metal. The metallic nature of the M_3S_4-type phases is further supported by the almost linear temperature dependence of |S|. By contrast, the Seebeck coefficient of the semiconducting phases ($x \leq 0.75$) does not follow the 1/T dependence expected for a conventional broad-band semiconductor.[28] Indeed for materials with x=0.2 and 0.3, |S| increases with temperature, which is the behaviour expected for a metal. Similar metal-like behaviour of S has been observed previously in semiconducting $NiCr_2S_4$[29] and has been attributed to a constant carrier concentration and thermally-activated mobility. In the present case the activated mobility is likely to arise from carrier localisation due to disorder

associated with cation substitution. As the vanadium content is increased across the M_2S_3 region, in addition to the decrease in the absolute value of the Seebeck coefficient, S(T) shows a much weaker temperature dependence and a change in sign of dS/dT is observed at *ca.* 200K, suggesting that more than one conduction mechanism may be operative.[30] This may also explain why S(T) does not follow the $T^{1/2}$ dependence expected for a variable-range-hopping semiconductor.

The zfc and fc magnetic susceptibility data for all phases overlie each other to the lowest temperature studied (Figure 11). At high temperatures, the susceptibility data follow a Curie-Weiss law. The Curie constant of $V_{0.1}Cr_{1.9}S_3$, determined as 3.52(2) cm^3 K mol^{-1} (Table 5), is in good agreement with the value of 3.66 cm^3 K mol^{-1} calculated assuming spin-only behaviour of localised Cr^{3+} and V^{3+} ions, and leads to an effective magnetic moment per cation of 3.75(1) μ_B. Progressive replacement of Cr^{3+}:d^3 by V^{3+}:d^2 would be expected to reduce the effective magnetic moment across the $V_xCr_{2-x}S_3$ series, leading to a minimum value of μ_{so} = 2.95 μ_B at $V_{1.8}Cr_{0.2}S_3$. Examination of the data in Table 5 reveals that, with increasing levels of vanadium incorporation, the measured moments are significantly reduced from spin-only values, that of $V_{0.75}Cr_{1.25}S_3$ attaining less than 55% of μ_{so}. Although the Weiss constants are relatively large and negative, indicative of predominantly antiferromagnetic exchange interactions, which would reduce the moment, we believe that the principal reason for the reduction in the effective magnetic moment is the increasing degree of electron delocalisation across the series, as revealed by the measurements of resistivity and Seebeck coefficient discussed above.

All materials, with the exception of $V_{0.75}Cr_{2.25}S_3$, show a sharp increase in susceptibility on cooling below a critical temperature, T_C. Across the M_2S_3 region, T_C decreases steadily with increasing vanadium content, suggesting a weakening of the magnetic exchange interactions as the phase boundary is approached, although the behaviour of the M_3S_4 phases is less systematic. The metallic nature of the M_3S_4-type phases leads to lower susceptibilities at low temperature than observed for the semiconducting M_2S_3-type materials.

Whilst the increase in magnetic susceptibility on cooling below T_C could be indicative of ferromagnetic ordering of moments, the negative Weiss constants reveal that the dominant magnetic exchange interactions are antiferromagnetic in origin. This suggests that the transition to long-range magnetic order involves a ferrimagnetic state, in which the spontaneous magnetisation arises from incomplete cancellation of ordered moments. Further support for this view is provided by the field-dependence of the magnetization at 5K (Figure 12). The saturated moments per cation (μ_{sat}), determined by extrapolation to infinite field of M *vs*. 1/H (Table 3), for materials with M_2S_3-type structures are considerably lower than those expected for ferromagnetic ordering of localised ions. The latter would lie in the range 2.9 – 2.1 μ_B, depending on vanadium content. The small measured saturated moments of <0.25 μ_B are consistent with ferrimagnetism. This is similar to the behaviour of the end-member phase, Cr_2S_3, the magnetic structure of which consists of three magnetic sublattices.[31] In the magnetically ordered phase, moments on two of the sublattices are coupled parallel to each other and are aligned antiparallel to the third sublattice, which

has twice the multiplicity. In Cr_2S_3, all cations have identical spin, and therefore ordering should produce a complete cancellation of the moments and no spontaneous magnetisation. The small ordered moment of $0.04\mu_B$ of Cr_2S_3 appears to result from spin-canting.[32] In the $V_xCr_{2-x}S_3$ ($0<x\leq0.75$) materials reported here, preferential incorporation of vanadium at a particular cation site, as established by structural analysis, removes the equivalence of the ordered moments associated with the three sub-lattices, leading to an increase in the saturated moment, even in the absence of spin-canting, but the values remain significantly less than those expected for ferromagnetic order. The values of the saturated moment for materials with M_3S_4-type structures are, at a few hundredths of a Bohr magneton, an order of magnitude lower than those of M_2S_3-type materials. This is again consistent with the metallic nature of materials in this compositional region.

In conclusion, we have shown that the ordered defect structure of Cr_2S_3 is retained on substitution of chromium by vanadium up to a composition of $V_{0.75}Cr_{1.25}S_3$. Although semiconducting behaviour persists throughout this composition range, the resistivity decreases progressively with increasing vanadium content. In Cr_2S_3, intralayer cation-cation separations are greater than the estimated minimum distance for direct t_{2g}-t_{2g} overlap (R_C) and, therefore, these interactions are weak. Consequently, t_{2g} levels that are essentially localised are separated by a band gap from an empty narrow band resulting from admixture of cation e_g states with anion s/p levels. Substitution of Cr^{3+}:d^3 with V^{3+}:d^2 introduces holes into the t_{2g} levels and also causes band broadening through direct cation-cation interactions. The diffraction data

indicate that such interactions are likely to be associated predominantly with sites in the fully occupied layer, which are preferentially occupied by vanadium cations as the level of substitution increases. The fall in resistivity may therefore be associated with the increased delocalisation of charge carriers, which is reflected in the increase in ξ across the series. Furthermore, substitution leads to mixed conduction, in which both holes and electrons contribute to the charge transport, leading to a Seebeck coefficient which reflects the conductivity-weighted sum of two contributions of opposite sign, whose absolute value decreases with increasing vanadium content. At higher levels of vanadium substitution, both resistivity and Seebeck coefficient data are indicative of metallic properties. The change to metallic behaviour is marked by a change to a Cr_3S_4-type structure, the symmetry of which permits the formation of zigzag cation chains in which cations are separated by distances of *ca*. 3Å. The existence of such chains appears to be closely linked to metallisation in ordered defect phases. An increasing level of electron delocalisation is also evident in the magnetic properties, which reveal a decrease in effective magnetic moment as the level of vanadium incorporation increases. The magnetic data also suggest that in each of the single-phase regions, a transition to a long-range magnetically-ordered state occurs at low temperatures. Investigation of the nature of this magnetically-ordered state and its evolution with composition will require neutron diffraction measurements at low temperatures.

Acknowledgements

We wish to thank the CCLRC Centre for Materials Physics and Chemistry and Heriot-Watt University for financial support to TEE.

Supplementary material

Final observed, calculated and difference X-ray and neutron powder diffraction profiles for $V_xCr_{2-x}S_3$ ($0.3 \leq x \leq 1.8$) are available.

References

(1) Tilley, R.J.D. Crystallography and Crystal Chemistry of Materials with Layered Structures; Levy F., Ed. Reidel: Dordrecht, pp 127-184, 1979.

(2) Vaughan, D.J.; Craig, J.R. Mineral Chemistry of Metal Sulphides; Cambridge University Press: Cambridge, 1978.

(3) Kjeshus, A.; Pearson, W.B. *Prog. Solid State Chem.*, **1964**, *1*, 83.

(4) Wold, A.; Dwight, K. Solid State Chemistry: Synthesis, Structure and Properties of Selected Oxides and Sulfides; Chapman and Hall: New York, ch. 11, 1993.

(5) Rao, C.N.R.; Pisharody, K.P.R. *Prog. Solid State Chem.*, **1979**, *10*, 207.

(6) Jellinek, F. *Acta Cyrstallogr.*, **1957**, *10*, 620.

(7) Oka, Y.; Kosuge, K.; Kachi, S. *J. Solid State Chem.*, **1978**, *23*, 11.

(8) Vaqueiro, P.; Powell, A.V. *Chem. Mater.*, **2000**, *12*, 2705.

(9) Haraldsen, H. ; Neuber, A. *Z. anorg. u. allgem. Chem*. **1937**, *234*, 337.

(10) Yuzuri, M. ; Nakamura, Y. *J. Phys. Soc. Japan*, **1964**, *19*, 1350.

(11) Van Bruggen, C. F.; Vellinga, M. B.; Haas, C. J. *J. Solid State Chem.*, **1970**, *2*, 303.

(12) Vaqueiro, P.; Powell, A.V.; Coldea, A.I.; Steer, C.A.; Marshall, I.M.; Blundell, S.J.; Singleton, J.; Ohtani, T. *Phys. Rev. B.,* **2001**, *64*, 132402.

(13) Colgan D.C.; Powell, D.C. *Mater. Sci. Forum*, **2001**, *278*, 686.

(14) Powell, A.V.; Colgan, D.C.; Vaqueiro, P. *J. Mater. Chem.*, **1999**, *9*, 485.

(15) Powell, A.V.; Vaqueiro, P. ; McDowall, A. *Solid State Ionics*, **2004**, *172*, 469.

(16) Colgan, D.C. ; Powell, A.V. *Mater. Sci. Forum*, **1998**, *278*, 686.

(17) David, W. I. F.; Johnson, M. W.; Knowles, K. J.; Moreton-Smith, C. M.; Crisbie, G. D.; Campbell, E. P.; Graham, S. P.; Lyall, J. S. Rutherford Appleton Laboratory Report, RAL-86-102, 1986.

(18) Larson, A. C.; von Dreele, R. B. *General Structure Analysis System*; Los Alamos Laboratory: Los Alamos, NM 87545, Report LAUR 85-748, 1994.

(19) Rowe, D. M., *CRC Handbook of Thermoelectrics*. CRC press: New York, 1995.

(20) Colgan, D. C.; Powell, A. V., *J. Mater. Chem.* **1996,** *6*, 1579.

(21) Vaqueiro, P.; Bold, M.; Powell, A.V.; Ritter, C.; *Chem. Mater.*, **2000**, *12*, 1034.

(22) Powell, A.V.; McDowall, A.D.; Vaqueiro, P.; Smith, R.I.; Ohtani, T.; Okuya, Y.; *J. Mater. Chem*, **2004**, *14*, 3051.

(23) van Bruggen, C. F.; Vellinga, M. B.; Haas, C. J., *J. Solid State Chem.* **1970,** *2*, 303.

(24) Mott, N. F., *J. Non-Cryst. Solids* **1968,** *1*, 1.

(25) Mott, N. F., *Metal-Insulator Transitions*. Taylor&Francis: London, 1990.

(26) Elliot, S. R., *The Physics and Chemistry of Solids*. Wiley: New York, 1998.

(27) Dijkstra, J.; Bruggen, C. F. V.; Haas, C.; Groot, R. A. D., *J. Phys.:Condens. Matter.* **1966,** *1*, 9163.

(28) Mott, N. F.; Davis, E. A., *Electronic Process in Non-Crystalline Materials, 2nd Edition*. Clarendon Press: Oxford, 1979.

(29) Powell, A. V.; Vaqueiro, P.; Ohtani, T., *Phys. Rev. B.* **2005,** *71*, 125120.

(30) Hamnett, A., *Solid-State Chemistry:Techniques*. A. K. Cheetham, P. Day ed.; Clarendon Press: Oxford, 1987; p 279.

(31) Popma, T. J. A.; Haas, C.; van Laar, B., *J. Phys. Chem. Solids* **1971,** *32*, 581.

(32) Bertaut, E.F.; Cohen, J.; Lambert-Andron, B.; Mollard, P., *J. Phys. (Paris)* **1968**, *29*, 813.

Table 1: Final Refined Parameters for Materials 0<x<0.75 with the Rhombohedral Cr_2S_3 Structure (space group $R\bar{3}$)[a]

		x in $V_xCr_{2-x}S_3$			
		0.2	0.3	0.4	0.6
	a /Å	5.9275(1)	5.9272(1)	5.9193(1)	5.9151(1)
	c /Å	16.7028(1)	16.7325(2)	16.7416(2)	16.7844(3)
(M(1))	SOF(V)	0.275(-)	0.358(-)	0.378(-)	0.439(-)
	SOF(Cr)	0.725(-)	0.642(-)	0.622(-)	0.561(-)
	B/Å^2	0.35(1)	0.33(1)	0.32(1)	0.25(1)
[M(2)]	SOF(V)	0.047(4)	0.106(4)	0.171(6)	0.268(8)
	SOF(Cr)	0.953(4)	0.894(4)	0.829(6)	0.732(8)
	B/Å^2	0.35(1)	0.33(1)	0.32(1)	0.25(1)
[M(3)]	SOF(V)	0.039(2)	0.068(2)	0.125(3)	0.247(4)
	SOF(Cr)	0.961(2)	0.932(2)	0.875(3)	0.753(4)
	B/Å^2	0.35(1)	0.33(1)	0.32(1)	0.25(1)
	z	0.3265(1)	0.3261(1)	0.3263(1)	0.3290(1)
S(1)	x	0.3384(3)	0.3388(2)	0.3391(3)	0.3395(5)
	y	-0.0046(3)	-0.0052(3)	-0.0045(3)	-0.0049(5)
	z	0.2523(1)	0.2525(1)	0.2524(1)	0.2523(1)
	B/Å^2	0.39(1)	0.37(1)	0.41(1)	0.47(1)
Rwp	X-ray	12.51%	14.14%	13.37%	17.61%
	neutron	1.40%	1.30%	1.79%	2.73%
χ^2		1.06	1.27	1.18	2.35

[a] Parentheses and square brackets denote cation sites in the vacancy and fully occupied layers respectively. (M(1)) on 3(b) (0,0,½); [M(2)] on 3(a) (0,0,0); [M(3)] on 6(c) 0,0,z) and S(1) on 18(f) (x,y,z).

Table 2: Final Refined Parameters for Materials ($1.6 \leq x \leq 1.8$) with the Monoclinic Cr_3S_4 Structure (space group I2/m)[a]

		x in $V_xCr_{2-x}S_3$	
		1.6	1.8
	a /Å	5.8228(1)	5.8158(2)
	b /Å	3.2978(1)	3.2841(1)
	c /Å	11.2497(3)	11.2868(4)
	β (deg)	91.440(3)	91.488(3)
(M(1))	SOF(V)	0.426(4)	0.525(4)
	SOF(Cr)	0.240(4)	0.142(4)
	B/Å^2	0.98(8)	1.31(12)
[M(2)]	SOF(V)	0.853(2)	0.937(2)
	SOF(Cr)	0.147(2)	0.063(2)
	x	-0.030(1)	-0.0348(7)
	z	0.257(1)	0.2564(5)
	B/Å^2	0.98(8)	1.31(12)
S(1)	x	0.3381(3)	0.3388(2)
	z	0.3650(1)	0.3645(1)
	B/Å^2	0.48(1)	0.39(1)
S(2)	x	0.3372(2)	0.3364(2)
	z	0.8856(1)	0.8857(1)
	B/Å^2	0.48(1)	0.39(1)
Rwp	X-ray	15.11%	13.70%
	neutron	1.07%	1.21%
χ^2		1.88	1.59

[a] Parentheses and square brackets denote cation sites in the vacancy and fully occupied layers respectively. (M(1)) on 2(a) (0,0,0); [M(2)] on 4(i) (x,0,z); S(1) and S(2) on 4(i) (x,0,z).

Table 3: Selected bond distances (Å) and angles (°) for $V_xCr_{2-x}S_3$ phases (M_2S_3)

	x in $V_xCr_{2-x}S_3$			
bond	0.2	0.3	0.4	0.6
M(1)-S	2.405(1) × 6	2.405(1) × 6	2.405(1) × 6	2.403(2) × 6
M(2)-S	2.394(1) × 6	2.394(1) × 6	2.391(1) × 6	2.392(3) × 6
M(3)-S	2.369(1) × 3	2.370(1) × 3	2.370(1) × 3	2.397(2) × 3
	2.427(1) × 3	2.427(1) × 3	2.427(1) × 3	2.398(2) × 3
M(1)-M(3)	2.898(1) × 2	2.908(1) × 2	2.908(1) × 2	2.870(3) × 2
M(2)-M(3)	3.424(1) × 6	3.424(1) × 6	3.420(1) × 6	3.416(1) × 6
M(3)-M(3)	3.430(1) × 3	3.430(1) × 3	3.426(1) × 3	3.418(1) × 3
S-M(1)-S	88.25(3) × 6	87.99(3) × 6	88.03(4) × 6	87.84(6) × 6
	91.74(3) × 6	92.00(3) × 6	91.97(4) × 6	92.16(6) × 6
S-M(2)-S	91.19(4) × 6	91.22(4) × 6	91.05(4) × 6	90.91(6) × 6
	88.81(4) × 6	88.78(4) × 6	88.95(4) × 6	89.09(6) × 6
S-M(3)-S	95.15(4) × 3	95.41(4) × 3	95.21(4) × 3	93.90(9) × 3
	88.73(4) × 3	88.68(4) × 3	88.86(4) × 3	89.09(9) × 3
	88.60(7) × 3	88.58(7) × 3	88.59(7) × 3	88.82(12) × 3
	87.23(4) × 3	87.01(4) × 3	87.03(5) × 3	88.04(9) × 3

Table 4: Selected bond distances (Å) and angles (°) for $V_xCr_{2-x}S_3$ phases (M_3S_4)

	x in $V_xCr_{2-x}S_3$	
bond	1.6	1.8
M(1)-S(1)	2.417(1) × 4	2.416(1) × 4
M(1)-S(2)	2.374(1) × 2	2.372(1) × 2
mean M(1)-S	2.40	2.40
M(2)-S(1)	2.439(6)	2.464(5)
	2.436(5) × 2	2.437(4) × 2
M(2)-S(2)	2.337(5) × 2	2.333(4) × 2
	2.372(6)	2.345(5)
mean M(2)-S	2.61	2.60
M(1)-M(1)	3.298(1) × 2	3.284(1) × 2
M(1)-M(2)	2.902(8) × 2	2.906(5) × 2
M(2)-M(2)	3.298(1) × 2	3.284(1) × 2
	3.045(10) × 2	2.994(7) × 2
	3.664(10) × 2	3.704(7) × 2
S(1)-M(1)-S(1)	86.05(6) × 2	85.62(5) × 2
	93.95(6) × 2	94.38(5) × 2
S(1)-M(1)-S(2)	88.52(5) × 4	88.15(4) × 4
	91.48(5) × 4	91.85(4) × 4
S(1)-M(2)-S(1)	82.53(17) × 2	81.85(12) × 2
	85.19(23)	84.71(16)
S(1)-M(2)-S(2)	91.99(4) × 2	92.21(5) × 2
	88.12(22) × 2	88.25(17) × 2
	89.54(22) × 2	89.06(16) × 2
S(2)-M(2)-S(2)	99.43(18) × 2	100.42(14) × 2
	89.76(26)	89.47(18)

Table 5: Parameters derived from magnetic susceptibility data for $V_xCr_{2-x}S_3$ ($0.1 \leq x \leq 1.8$)

	x in $V_xCr_{2-x}S_3$								
	0.1	0.2	0.4	0.5	0.6	0.75	1.6	1.7	1.8
Data Range for fit /K	130-300	160-300	155-300	180-300	160-300	180-300	170-300	170-300	170-300
$C/cm^3.Kmol^{-1}$	3.52(2)	3.00(4)	2.49(2)	2.35(2)	1.61(1)	0.89(2)	0.96(1)	1.36(3)	1.10(1)
Θ/K	-363(3)	-208(6)	-131(3)	-106(2)	-134(1)	-195(9)	-375(7)	-201(9)	-303(6)
T_C K	118	112	110	100	102	100	90	108	95
μ_{exp} per M cation	3.75(1)	3.47(2)	3.16(1)	3.06(1)	2.54(1)	1.89(1)	1.96(1)	2.33(1)	2.10(1)
μ_{so}	3.83	3.78	3.69	3.64	3.58	3.52	3.07	3.00	2.95
Saturation magnetization/μ_B	0.12(1)	0.25(1)	0.23(1)	0.23(1)	0.12(1)	0.052(1)	0.018(1)	0.082(1)	0.034(1)

Table 6: Parameters extracted from variable-range-hopping fits with $\nu = 1/4$

x in $V_xCr_{2-x}S_3$	Data range for fit/K	ρ_0/Ωcm	$T_0/10^4$ K	ξ/Å
0.25	300-80	2.09	79.46	1.24
0.4	180-80	2.01	54.18	1.41
0.5	300-80	3.46	8.65	2.60
0.75	300-80	2.52	2.44	3.97

FIGURE CAPTIONS

Figure 1	The defect ordering scheme within the partially-occupied layers (*ab* plane) of Cr_2S_3 (left) and Cr_3S_4 (right). Solid circles represents cations, open circles represent vacancies.
Figure 2	The Cr_2S_3 structure. Grey octahedra represent MS_6 units in the fully occupied layer and the solid circles represent cations in the partially occupied layer.
Figure 3	The Cr_3S_4 structure. Cations in the ordered defect layer are shown as solid circles and cations in the fully occupied layer lie at the centre of shaded MS_6 octahedra, which share edges to form a layer of stoichiometry MS_2.
Figure 4	Final observed (crosses), calculated (upper full line) and difference (lower full line) profiles for (a) $V_{0.2}Cr_{1.8}S_3$ and (b) $V_{1.8}Cr_{0.2}S_3$ (X-ray data : upper plot, neutron data : lower plot). Reflection positions are marked.
Figure 5	Compositional variation of the fraction of available vanadium that resides in the fully occupied layer, V_F, in $V_xCr_{2-x}S_3$ ($0<x<2$). The sequential nature of the refinement for M_2S_3-type phases precludes inclusion of error bars (see text), whilst those for M_3S_4-type phases lie within the points.
Figure 6	Compositional dependence of (a) the volume, normalised to that per M_2S_3 formula unit in order to facilitate comparison between the two structure types and (b) the lattice

	parameters of the primitive hexagonal sub-cell for the two single-phase regions of $V_xCr_{2-x}S_3$. In (b) *a* and *b* parameters in the M_2S_3-type structure are denoted by solid circles and by open and solid circles respectively for the M_3S_4-type structure; solid squares denote, *c*, for both structure types. Error bars lie within the points
Figure 7	Temperature dependence of the electrical resistivity of $V_xCr_{2-x}S_3$ phases.
Figure 8	An Arrhenius plot showing the linear fits to data for $V_xCr_{2-x}S_3$ (x = 0.1 and 0.2).
Figure 9	Fit to the resistivity data for $V_xCr_{2-x}S_3$ ($0.25 \leq x \leq 0.75$) showing the $T^{-1/4}$ dependence of $\ln(\rho)$. The straight lines are the fit to the variable-range-hopping expression of equation (1) over the range of temperatures given in Table 5.
Figure 10	Seebeck coefficient data for $V_xCr_{2-x}S_3$ ($0.2 \leq x \leq 1.8$) collected over the temperature range $80 \leq T/K \leq 350$
Figure 11	Zero-field-cooled (zfc) and field-cooled (fc) molar magnetic susceptibilities for $V_xCr_{2-x}S_3$ ($0.1 \leq x \leq 1.8$) phases measured in a field of 1000G. The insets show the fit to the Curie-Weiss expression.
Figure 12	Magnetization per cation as a function of field for $V_xCr_{2-x}S_3$ ($0.1 \leq x \leq 1.8$) phases at 5K.

FIGURE(S)

Figure 1

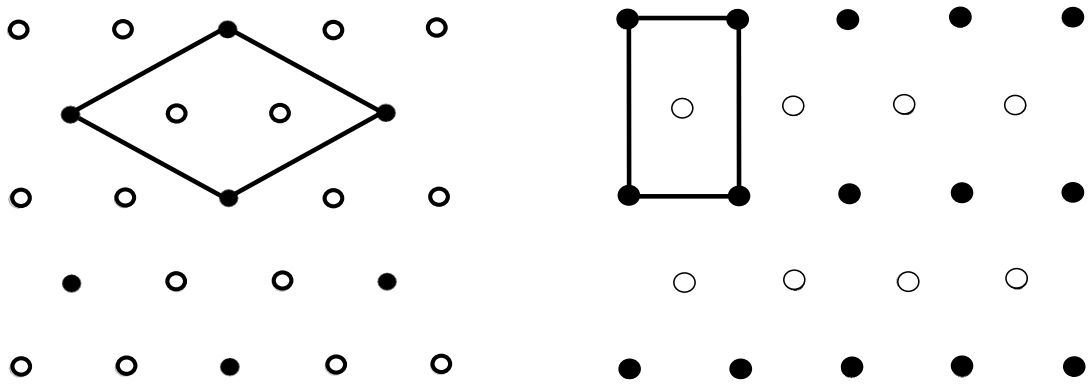

Figure 2

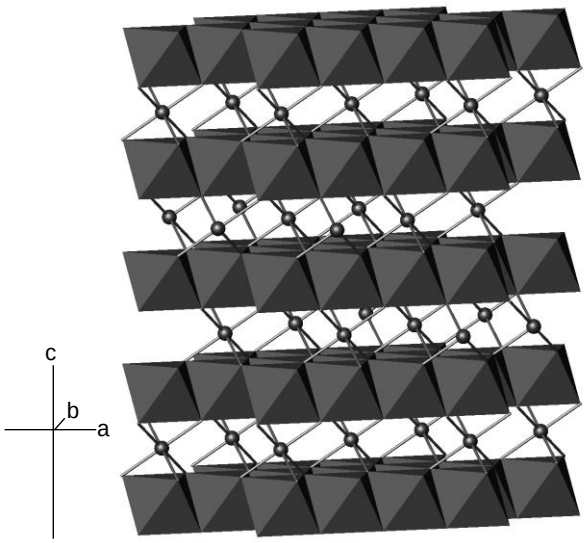

Figure 3

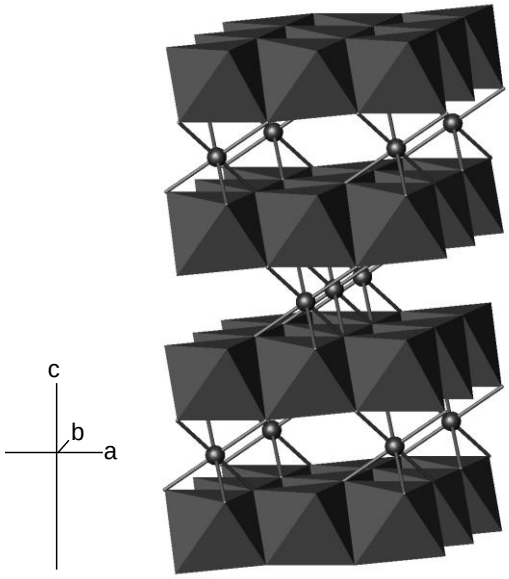

Figure 4

a)

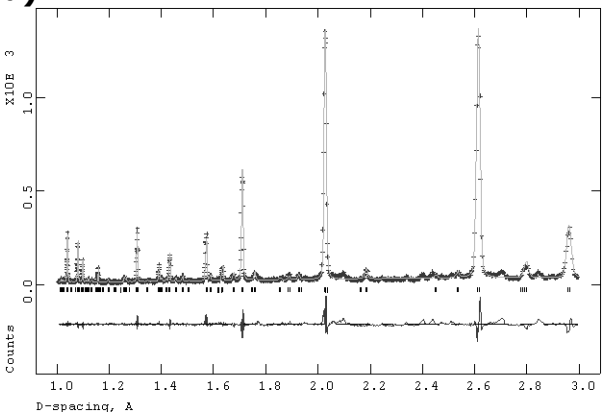
X10E 3
1.0
0.5
0.0
Counts
1.0 1.2 1.4 1.6 1.8 2.0 2.2 2.4 2.6 2.8 3.0
D-spacing, A

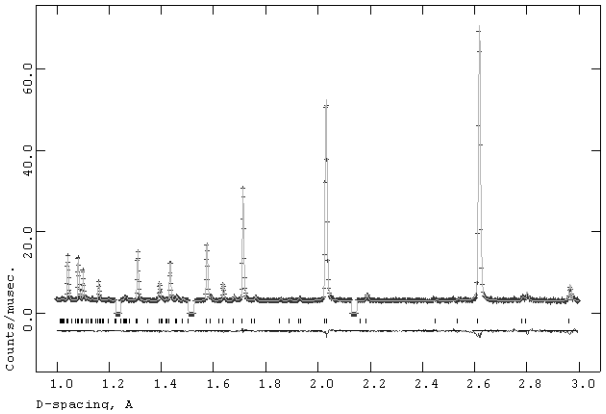
60.0
40.0
20.0
0.0
Counts/musec.
1.0 1.2 1.4 1.6 1.8 2.0 2.2 2.4 2.6 2.8 3.0
D-spacing, A

b)

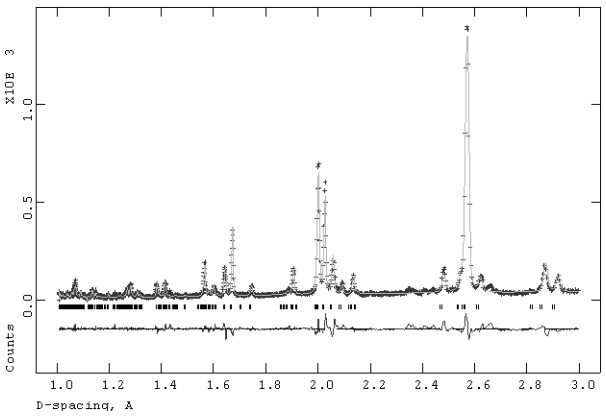
X10E 3
1.0
0.5
0.0
Counts
1.0 1.2 1.4 1.6 1.8 2.0 2.2 2.4 2.6 2.8 3.0
D-spacing, A

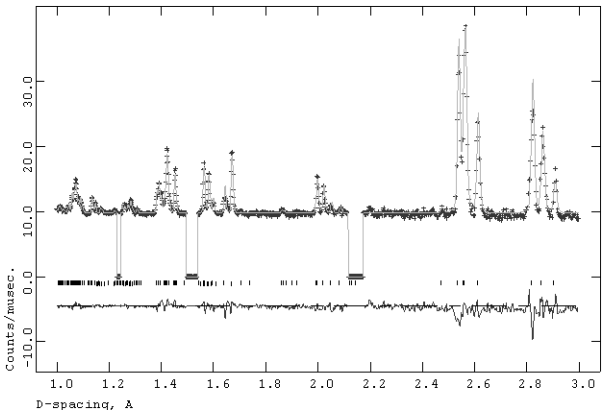
30.0
20.0
10.0
0.0
-10.0
Counts/musec.
1.0 1.2 1.4 1.6 1.8 2.0 2.2 2.4 2.6 2.8 3.0
D-spacing, A

Figure 5

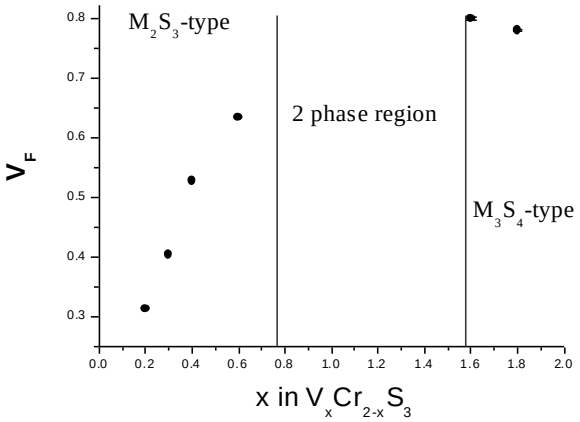
M2S3-type
2 phase region
M3S4-type
VF
x in VxCr2-xS3
0.8
0.7
0.6
0.5
0.4
0.3
0.0
0.2
0.4
0.6
0.8
1.0
1.2
1.4
1.6
1.8
2.0

Figure 6

a)

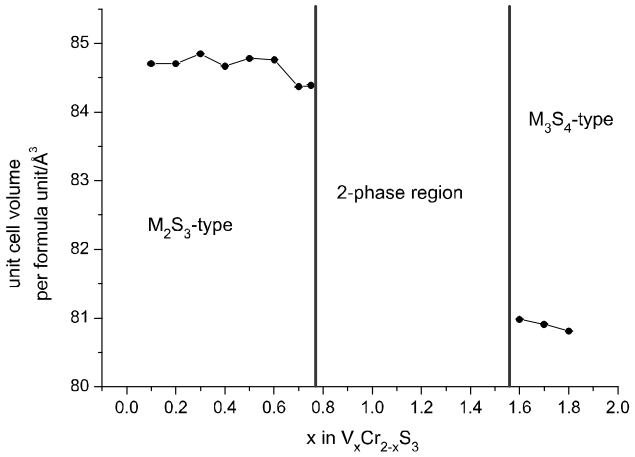
unit cell volume per formula unit/Å^3
85
84
83
82
81
80
0.0
0.2
0.4
0.6
0.8
1.0
1.2
1.4
1.6
1.8
2.0
x in $V_xCr_{2-x}S_3$
M_2S_3-type
2-phase region
M_3S_4-type

b)

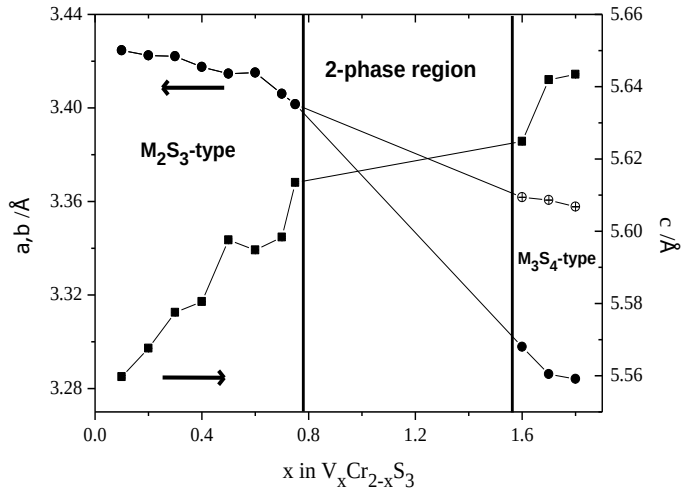
a,b /Å
c /Å
3.44
3.40
3.36
3.32
3.28
5.66
5.64
5.62
5.60
5.58
5.56
0.0
0.4
0.8
1.2
1.6
x in $V_xCr_{2-x}S_3$
2-phase region
M_2S_3-type
M_3S_4-type

Figure 7

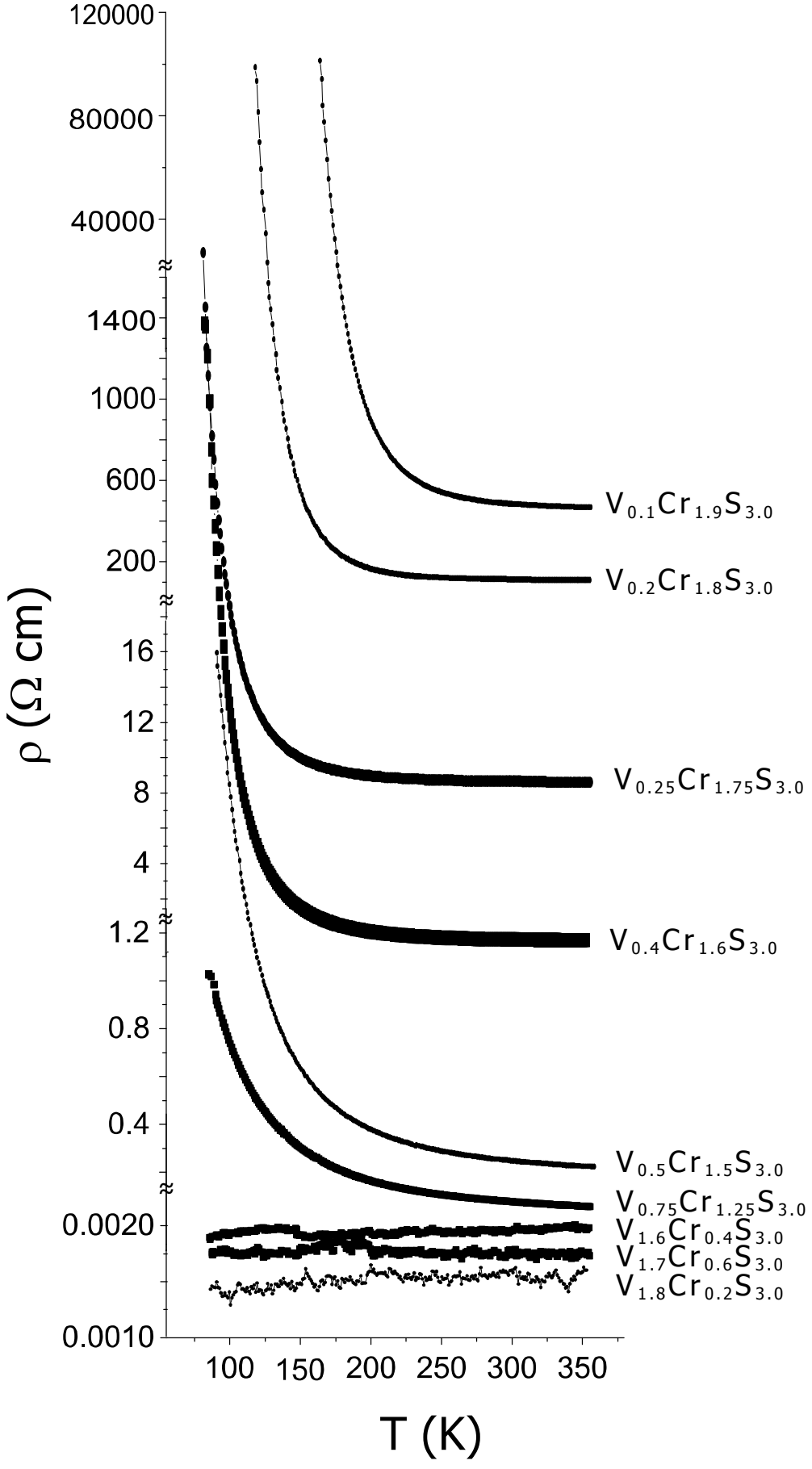
120000
80000
40000
1400
1000
600
200
16
12
8
4
1.2
0.8
0.4
0.0020
0.0010
ρ (Ω cm)
100
150
200
250
300
350
T (K)
V0.1Cr1.9S3.0
V0.2Cr1.8S3.0
V0.25Cr1.75S3.0
V0.4Cr1.6S3.0
V0.5Cr1.5S3.0
V0.75Cr1.25S3.0
V1.6Cr0.4S3.0
V1.7Cr0.6S3.0
V1.8Cr0.2S3.0

Figure 8

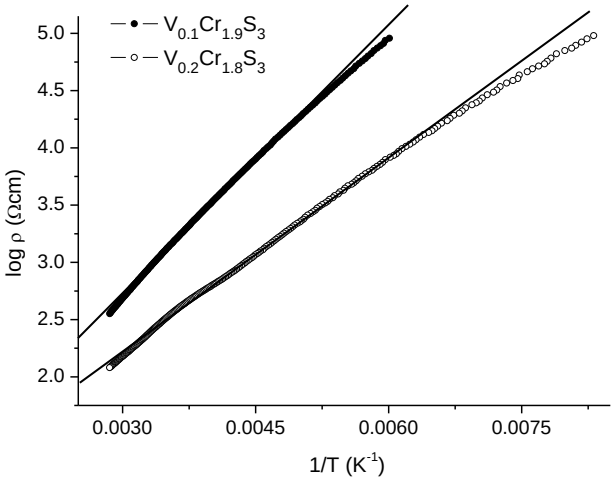
V0.1Cr1.9S3
V0.2Cr1.8S3
log ρ (Ωcm)
1/T (K-1)
5.0
4.5
4.0
3.5
3.0
2.5
2.0
0.0030
0.0045
0.0060
0.0075

Figure 9

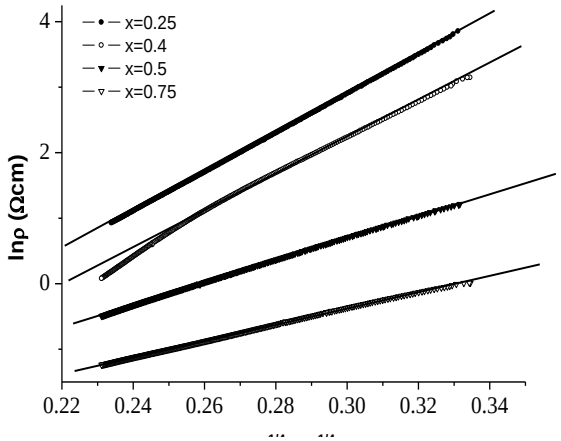

Figure 10

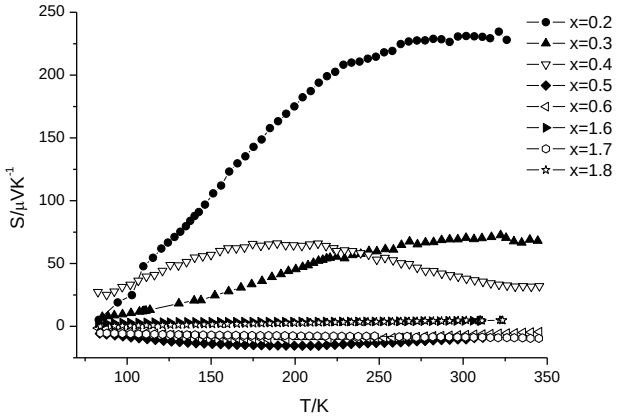
250
200
150
100
50
0
S/μVK-1
100
150
200
250
300
350
T/K
x=0.2
x=0.3
x=0.4
x=0.5
x=0.6
x=1.6
x=1.7
x=1.8

Figure 11

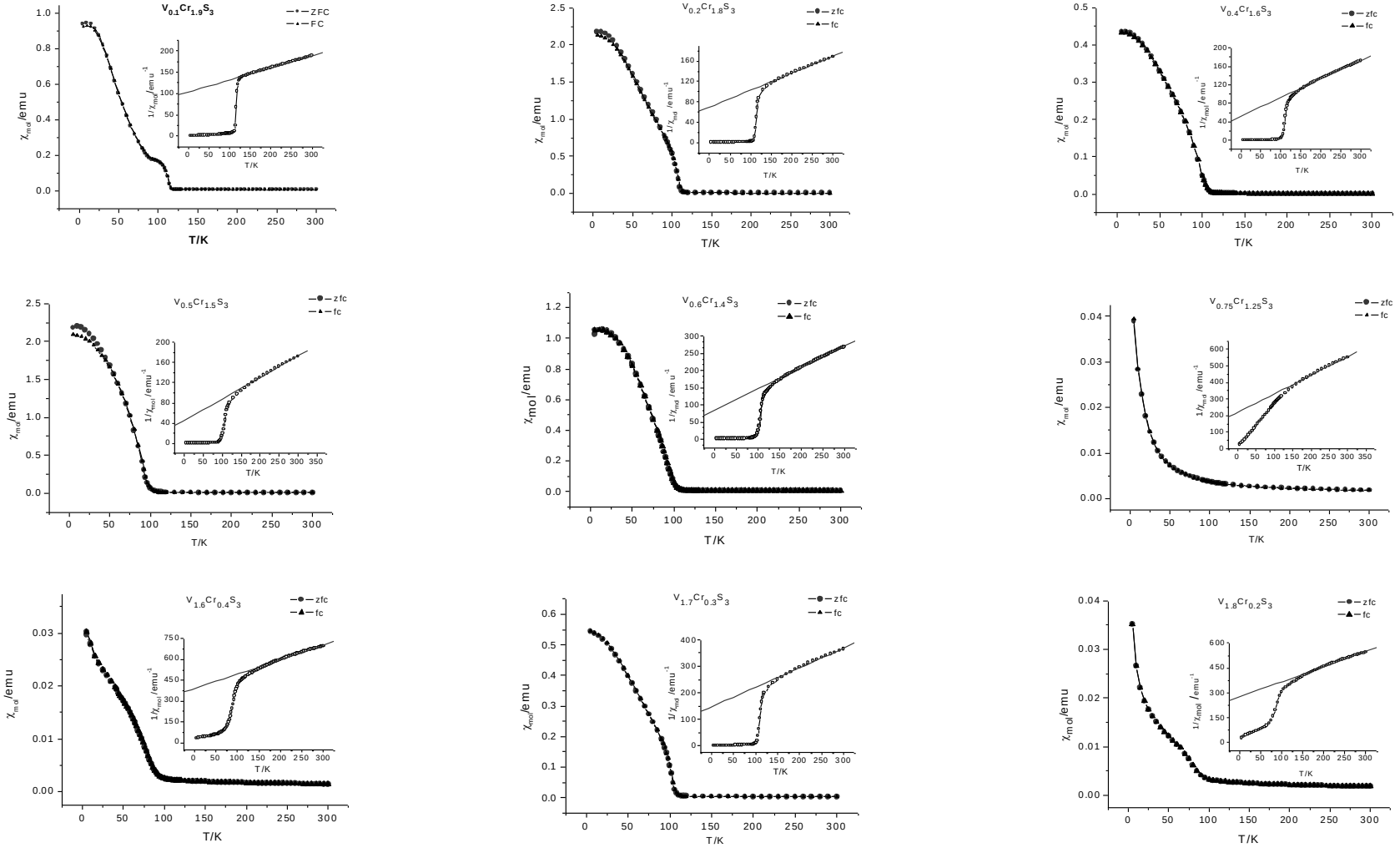
V0.1Cr1.9S3
ZFC
FC
V0.2Cr1.8S3
zfc
fc
V0.4Cr1.6S3
zfc
fc
V0.5Cr1.5S3
zfc
fc
V0.6Cr1.4S3
zfc
fc
V0.75Cr1.25S3
zfc
fc
V1.6Cr0.4S3
zfc
fc
V1.7Cr0.3S3
zfc
fc
V1.8Cr0.2S3
zfc
fc
T/K

Figure 12

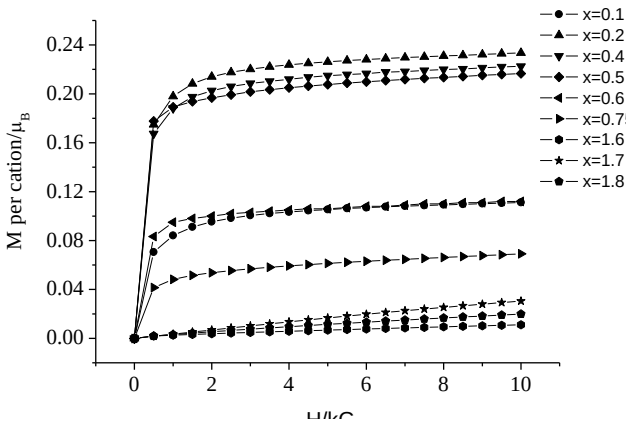
M per cation/μ_B
0.24
0.20
0.16
0.12
0.08
0.04
0.00
0
2
4
6
8
10
x=0.1
x=0.2
x=0.4
x=0.5
x=0.6
x=0.7
x=1.6
x=1.7
x=1.8